Full-field DIC-based model updating for localized parameter identification

Klemen Zaletelj[a], Janko Slavič[a,*], Miha Boltežar[a]

[a] *University of Ljubljana, Faculty of Mechanical Engineering, Aškerčeva 6, 1000 Ljubljana, Slovenia*

Cite as:
Klemen Zaletelj, Janko Slavič and Miha Boltežar, Full-field DIC-based model updating for localized parameter identification, Mechanical Systems and Signal Processing, Volume 164, February 2022, `https://doi.org/10.1016/j.ymssp.2021.108287`

Abstract

Identifying the local properties of a structure, either to perform structural health monitoring or to fine tune a numerical model, requires the updating of a large number of parameters. With a high spatial density, but a low dynamic range response information, high-speed-camera measurements have the potential to identify a large number of localized parameters. In contrast, accelerometer measurements provide low-spatial-density modal shapes, but a high dynamic range, and introduce the problem of mass loading. In this research, modal shapes from a high-speed camera are used, providing full-field response information about the observed structure and an over-determined optimization problem. Since the high-speed camera has a lower dynamic range than the accelerometer and the signal-to-noise ratio is low where the displacement amplitude is small, location-specific weighting methods were introduced. The numerical and real experiments showed that the accelerometer's positioning is important for successful updating, while with a high-speed-camera measurement this is not relevant. This research showed that due to the spatial over-determination, the model updating based on high-speed-camera data, was significantly better than the low-spatial-resolution, accelerometer-based approach.

*Corresponding author
Email address: `janko.slavic@fs.uni-lj.si` (Janko Slavič)

Keywords: full-field response, DIC, finite-element-model updating, localized parameters

1. Introduction

High-speed imaging has become a popular approach for both static and dynamic measurements because it is a non-contact method and provides full-field response information. Lucas and Kanade [1] developed an algorithm for tracking a pattern as it moves across the camera's sensor. Peters *et al.* [2] used the approach in the field of mechanics, where it is known as Digital Image Correlation (DIC) [3]. In the field of structural dynamics, Niezrecki *et al.* [4] reviewed the use of DIC and Baqersad *et al.* [5] reviewed the use of multiple optical methods. The 3D response of the structure is identified using multiple synchronized high-speed cameras [6]; however, Gorjup *et al.* [7] showed that, using frequency-domain triangulation, the 3D operational shapes of a linear, time-invariant system can be identified using a single high-speed camera. Renaud *et al.* [8] reconstructed the vibration shapes by combining a single camera footage and the finite-element model. Barone *et al.* [9] used a single camera and mirrors to create pseudo-stereo images of a target and used 3D DIC to identify the 3D displacements. Felipe-Sesé *et al.* [10] proposed a combination of fringe projection and DIC to identify the 3D modal shapes. Javh *et al.* [11] showed that the modal shapes can also be identified using a still camera as an integrator for the Fourier coefficients of an optical flow, while Gorjup *et al.* [12] extended the method to 3D deflection shapes. For operational modal analysis, Chang *et al.* [13] proposed compressed sensing using a full-field measurement, and an automated harmonic-signal-removal technique was presented by Hasan *et al.* [14]. Del Sal *et al.* [15] showed that the accuracy of the deflection shape measurements significantly rises with an increasing number of used cameras.

The use of high-speed cameras has significantly increased in the last two decades and the advances in technology make their use accessible in various applications. Huang *et al.* [16] proposed a pre-processing method for DIC on rotating structures and for high surface speeds, while Wollmann *et al.* [17] proposed motion blur suppression. Khadka *et al.* [18] used a DIC system, mounted on a semi-autonomous UAV, to monitor rotating wind turbines, Jiang *et al.* [19] used robust line-tracking photogrammetry to inspect a railway power line and Bhowmick *et al.* [20] measured the full-field time history of a continuous edge. Tarpø *et al.* [21] estimated the full-field strain of subsystems within a time-varying, non-linear system using modal expansion, while Chabrier *et al.* [22] used DIC measurements to characterize a vibro-impact absorber. With output-only data, Lu *et al.* [23] used vision modal analysis to identify the modal shapes.

The field of finite-element-model updating is well established and is still in active development. Friswell *et al.* [24] researched finite-element-model updating in detail and classified it into the direct and sensitivity-based methods. Recently, Zhu *et al.* [25] proposed a substructure-based sensitivity method to accelerate the convergence of model updating. Rezaiee-Pajand *et al.* [26] presented an innovative, sensitivity-based updating strategy using a combination of the modal kinetic energy and the modal strain energy. Girardi *et al.* [27] proposed a numerical method for finding a global minimum of the cost function. Wan *et al.* [28] used a global-sensitivity analysis to decide on the best parameters to update. Recently, Bayesian methods for finite-element-model updating have been researched for structural health monitoring [29] and including the damping data in the updating procedure [30]. Patelli *et al.* [31] compared the sensitivity and Bayesian model updating approaches and found that the updated parameters from both are similar; however, the Bayesian approach requires large computational resources, even when surrogate models are used [32]. The machine-learning approach to model updating is also gaining in popularity; Gaussian process emulation for the uncertain-parameter identification was presented by Zhou *et al.* [33], and a combination of machine-learning approaches was used by Xia *et al.* [34]. Seventekidis *et al.* [35] used deep-learning-based model updating to perform structural health monitoring.

The use of high-speed-camera measurements in finite-element-model updating has the benefit of a large number of degrees of freedom being measured simultaneously, which enables the identification of local mode-shape features and the use of local correlation indicators. To achieve a spatial density of information similar to a high-speed camera by using accelerometers can be time consuming and a large number of sensors must be used, requiring sensors position optimization [36] and adding mass to the structure. One of the first uses of high-speed cameras for model updating was by Wang *et al.* [37] who used Tchebichef moment descriptors to describe modal shapes. Ngan *et al.* [38] used DIC measurements to investigate the Zernike moment descriptors. Zanarini [39] compared the updating results when the experimental data are obtained using high-speed cameras with 3D DIC algorithm, SLDV and ESPI. While Rohe *et al.* [40] successfully used SLDV measurements in the updating procedure, Zanarini showed that the 3D DIC and ESPI approaches were superior to SLDV. Recently, Cuadrado *et al.* [41] used the sensitivity approach to update the parameters of a composite plate using a full-field vibration measurement; however, only three parameters were updated.

While the research of high-speed cameras usage in the updating procedure exists, the advantages of full-field structural response information to obtain an overdetermined optimization problem for updating a large number of localized parameters has previously not been extensively addressed. In this research, displacements, identified from a high-speed camera footage, are used to update a large number of unknown parameters and identify a localized anomaly on the structure. The influence of the number of measured degrees of freedom, modal-shape noise and measurements-location positioning (for accelerometer measurements) on the updated parameters is investigated with numerical and real experiments.

This manuscript is organized as follows. Section 2 presents the theoretical background of image-based displacement identification, full-field modal-parameter identification and finite-element-model updating. The Section 3 introduces the location-weighting to rely on data where noise is relatively small. Section 4 presents the real experiment along with the model updating-results. The conclusions are drawn in Section 5.

2. Theoretical background

The displacement identification from the high-speed-camera video, modal-parameter identification and sensitivity-based finite-element-model updating are discussed in this section.

2.1. Image-based displacement identification

The high-speed camera captures the sequential frames with light-intensity information for each pixel, which can be used to identify the displacements. To extract the displacement of a certain pixel, or a subset of pixels, a number of algorithms can be used. For the purposes of this research, a 2D DIC algorithm will be used, where only the rigid translations of the subsets are identified. At small deformations, it was found, that identifying only the translations significantly decreases the computation time and provides results with smaller noise (with respect to also identifying the distortion and rotation). DIC is based on an iterative algorithm, whose goal is to minimize the cost function S [3, 42], in our case:

$$S = \sum_{x} \sum_{y} \left(I_{\text{ref}}(x, y) - I(x + \Delta x, y + \Delta y) \right)^2, \tag{1}$$

where I_{ref} represents the intensities of the subset of pixels on the reference image (usually the first captured image) and I on the current image. When S is minimized, Δx and Δy represent the identified displacements of the subset on the current image with respect to the reference image in the horizontal and vertical directions, respectively. The spatial resolution is limited by the subset size. An overlap larger than 1/3 of a subsets does not, in general, increase the resolution further [43]; however, in this research it was found that a larger overlap did provide additional information. The practical aspects of modal testing using high-speed cameras were presented by Witt *et al.* [44].

To successfully identify the displacements using DIC, a pattern that moves along with the structure, must be present on the inspected surface. The pattern-quality measure was researched by Lecompte *et al.* [45] and Pan *et al.* [46]. With DIC algorithm, a speckle pattern is normally used, which is usually applied to the surface. Various pattern-application techniques were reviewed in [47].

In this research, a speckle pattern was generated using a Python package speckle-pattern [48]. The speckles are generated in a grid pattern where the user can choose the grid step and the speckle size. Additionally, the randomness of speckles position can be adjusted, as well as the variation in speckle sizes. The pattern was printed on a sticker [44] that was applied to the front surface of the structure, see Sec. 4.

2.2. Hybrid full-field experimental modal analysis

Recently, the most used technique for modal-parameter identification based on the frequency-response-function estimate is the Least-Squares Complex Frequency (LSCF) method [49] in combination with the Least-Squares Frequency Domain (LSFD) method [50, 51]. The FRF estimates, identified from the high-speed-camera measurement, are noisy, especially at higher frequencies where the displacements are usually small in comparison to the noise on the camera's sensor. Five bits (of the total twelve) represent the noise for the camera used in this research and the noise level is at 0.00035 px [52]; consequently, the LSCF pole identification is less reliable. A hybrid method, combining the high-dynamic-range acceleration measurement with the spatially dense high-speed-camera measurement, was proposed by Javh *et al.* [52]. With the hybrid method, the poles are identified using the LSCF method by fitting a rational polynomial function to the acceleration measurement data:

$$ {}_{\mathrm{acc}}\alpha_j(\omega) = \frac{\sum_r a_{j,r} \cdot \mathrm{e}^{-\mathrm{i}\, r\, \Delta t\, \omega}}{\sum_r b_r \cdot \mathrm{e}^{-\mathrm{i}\, r\, \Delta t\, \omega}}, \tag{2} $$

where j is the location index, r is the polynomial order, Δt is the time step in seconds and ω is the angular frequency. The denominator roots are poles of the function and are associated with the complex eigenvalues ${}_{\mathrm{acc}}\lambda_r$. To select the stable, physically meaningful poles, an increasing polynomial order is used and a stability chart is plotted [53]. ${}_{\mathrm{acc}}\lambda_r$ contains information about the r-th natural frequency, ω_r, and the damping, ζ_r :

$$ {}_{\mathrm{acc}}\lambda_r = -\zeta_r\, \omega_r \pm \mathrm{i}\, \omega_r \sqrt{1-\zeta_r^2}. \tag{3} $$

The identified complex eigenvalues ${}_{\mathrm{acc}}\lambda_r$ are then used in the LSFD method, where a polynomial is fitted to the camera FRF estimates, ${}_{\mathrm{cam}}\alpha_j(\omega)$:

$$ {}_{\mathrm{cam}}\alpha_j(\omega) = \sum_{r=1}^{N} \left(\frac{{}_rA_j}{\mathrm{i}\,\omega - {}_{\mathrm{acc}}\lambda_r} + \frac{{}_rA_j^*}{\mathrm{i}\,\omega - {}_{\mathrm{acc}}\lambda_r^*} \right) - \frac{A_{\mathrm{L}}}{\omega^2} + A_{\mathrm{U}}, \tag{4} $$

where ${}_rA_j$ is the modal constant for the r-th mode, at the j-th location and * denotes a complex conjugate. A_{L} and A_{U} are the lower and upper residuals, respectively, representing the influence of the modes below and above the observed frequency range. Spatially dense modal shapes are obtained because of the large number of locations j.

The LSCF and LSFD methods are implemented in the open-source Python package pyEMA [54].

2.3. Sensitivity-based finite-element-model updating

The sensitivity methods are based on solving a non-linear least-squares optimization problem using the Marquerdt approach [55], where a linearisation and iterative solving are used. The numerical model is compared to the measured values using the residual vector:

$$ \delta\mathbf{z} = \mathbf{z}_{\mathrm{m}} - \mathbf{z}_j, \tag{5} $$

where $\mathbf{z}_\mathrm{m}$ is the vector of the measured/reference data and $\mathbf{z}_j$ is the vector of the corresponding data from the numerical simulation in the j-th iteration. Any type of response data that can be obtained from both the measurement and the numerical model can be included in the residual vector. The eigenvalues and modal shapes are the most commonly used; however, the FRFs can also be included [56, 57].

When computing the residual vector, problems of mode matching and scaling emerge. Mode matching is necessary when not all the modes that are represented in the numerical model are identified, *e.g.*, torsional and (for 2D DIC) out-of-plane modes, meaning that a simple sorting of eigenvalues by size and comparing the first few shapes is not correct. The established approach is to use the Modal Assurance Criterion (MAC) [58] to compute the MAC matrix. The elements in the matrix with a value close to one, represent the matching modal shapes. It is important to note here, that with higher, geometrically complex modal shapes, a small number of measured points can cause false matching due to spatial aliasing, a problem that does not occur with a full-field measurement. A good indicator for evaluating a sufficient number of measurement points is the auto-MAC matrix, where the goal is a diagonal matrix, see Fig. 1. The problem of scaling must also be addressed

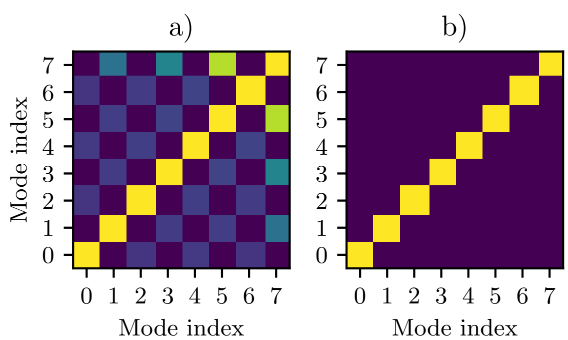

Figure 1: Auto MAC matrix for a) 9 measured points and b) 160 measured points in the modal shape.

when comparing the modal shapes, since the scaling of measured and numerical shapes might not be consistent due to the different mass normalizations of the mode shapes, the consequence of an incorrect mass distribution in the numerical model. To scale the measured shapes to the numerical shapes and correct the 180° phase discrepancy, a Modal Scale Factor (MSF) [59] is used, see Fig. 2.

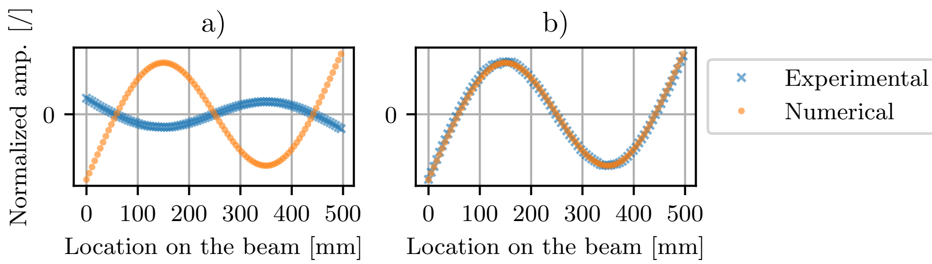

Figure 2: Scaling of modal shapes with the Modal Scale Factor. a) no scaling and b) with scaling.

To update the parameters of the numerical model, the error function is minimized:

$$J(\boldsymbol{\theta}) = \boldsymbol{\varepsilon}^T \cdot \boldsymbol{\varepsilon}, \tag{6}$$

where $\cdot$ denotes the matrix or vector multiplication, ^{T} denotes the transpose and $\boldsymbol{\theta}$ is a vector of parameters that are updated. $\boldsymbol{\varepsilon}$ is defined as:

$$\boldsymbol{\varepsilon} = \delta \mathbf{z} - \mathbf{S}_j \cdot \delta \boldsymbol{\theta} \tag{7}$$

where $\mathbf{S}_j$ is the sensitivity matrix, evaluated in the j-th iteration and $\delta\boldsymbol{\theta}$ is:

$$\delta \boldsymbol{\theta} = \boldsymbol{\theta}_j - \boldsymbol{\theta}_{j+1} \tag{8}$$

The sensitivity matrix $\mathbf{S}_j$ contains partial derivatives of all the data in $\mathbf{z}_j$ with respect to the updating parameters:

$$\mathbf{S}_j = \begin{bmatrix} \frac{\partial z_1}{\partial \theta_1}\Big|_{\theta=\theta_j} & \frac{\partial z_1}{\partial \theta_2}\Big|_{\theta=\theta_j} & \cdots \\ \frac{\partial z_2}{\partial \theta_1}\Big|_{\theta=\theta_j} & \frac{\partial z_2}{\partial \theta_2}\Big|_{\theta=\theta_j} & \cdots \\ \vdots & \vdots & \ddots \end{bmatrix}_{(n,m)}, \tag{9}$$

where n is the number of residuals in $\delta\mathbf{z}$ and m is the number of parameters to be updated. To compute the derivatives in $\mathbf{S}_j$, either an analytical evaluation or numerical perturbation can be used [60]. The analytical differentiation has the advantage of speed; however, parametrized matrices are not always available in finite-element solvers. On the other hand, the implementation of a numerical derivation requires multiple evaluations of the finite-element model. For large numbers of elements, the time of a single evaluation significantly increases; on a personal PC, the evaluation for 999 elements lasted for 0.15 seconds, while for 10 000 elements it lasted for 10 seconds. To address the problem of computation time, parallel computing can be used. In this research, the number of elements was relatively small (999 element) and the sensitivity matrix was computed numerically.

When the number of residuals n is larger than the number of updating parameters m, the system is over-determined and the approximation of the updating parameters in the next iteration, $j+1$, can be computed by minimizing Eq. (6) using the Marquardt approach:

$$\boldsymbol{\theta}_{j+1} = \boldsymbol{\theta}_j + \left[\mathbf{S}_j \cdot \mathbf{S}_j^T\right]^{-1} \cdot \mathbf{S}_j^T \cdot \left(\mathbf{z_m} - \mathbf{z}_j\right) \tag{10}$$

When the number of updating parameters m is larger than the number of residuals n, the updating parameters cannot be uniquely identified. The Tikhonov regularization [61] is used to obtain the solution with the minimal change in updating parameters. Information about the level of confidence for the initial estimate is written in the weighting matrix $\mathbf{W}_{\theta\theta}$, a diagonal matrix with reciprocal values of the estimated variances of the parameters, with a shape of $(n \times n)$. When the same weight is given to all of the updating parameters, the Tikhonov regularization corresponds to the L2 regularization [62]. Additionally, the measured data can be weighted to describe the noise and uncertainty. A diagonal matrix with reciprocal values of the variances of the measured data $\mathbf{W}_{\varepsilon\varepsilon}$, with a shape of $(m \times m)$, is constructed and the weighted least-squares solution can be computed. Combining the weighted least-squares solution with the Tikhonov regularization gives an approximation of the parameters in the iteration $j+1$:

$$\boldsymbol{\theta}_{j+1} = \boldsymbol{\theta}_j + \left[\mathbf{S}_j^T \cdot \mathbf{W}_{\varepsilon\varepsilon} \cdot \mathbf{S}_j + \mathbf{W}_{\theta\theta}\right]^{-1} \cdot \mathbf{S}_j^T \cdot \mathbf{W}_{\varepsilon\varepsilon} \cdot \left(\mathbf{z}_{\mathrm{m}} - \mathbf{z}_j\right) \tag{11}$$

Eq. (11) is also used for over-determined systems when one or more parameters have no effect on the residuals, when multiple parameters have the same effect or when the measurements are noisy.

In this research, noisy measurements are used and location-specific weighting of the modal shapes is introduced by Eq. (11), see Sec. 3. All of the parameters were given equal weight in $\mathbf{W}_{\theta\theta}$, chosen so that the Euclidean norm of $\mathbf{W}_{\theta\theta}$ was equal to the Euclidean norm of $\mathbf{W}_{\varepsilon\varepsilon}$.

3. Numerical research on the location-weighting of noisy data

In this section, the location-specific weighting of noisy data is investigated based on a numerical experiment. The effects of sensor position and noise level on the model updating are discussed.

The measurement was simulated using the reference numerical model, created by modelling a beam (Fig. 3) with 999 Euler-Bernoulli finite elements [63]. The density of the material, ρ, for the reference model was $7400\,\mathrm{kg/m^3}$ and the Young's modulus, E, was 180 GPa. To introduce a parameter variation, the Young's modulus was reduced (36 GPa) for elements at locations from 500 through 520. A free-free boundary condition was applied and no damping was included.

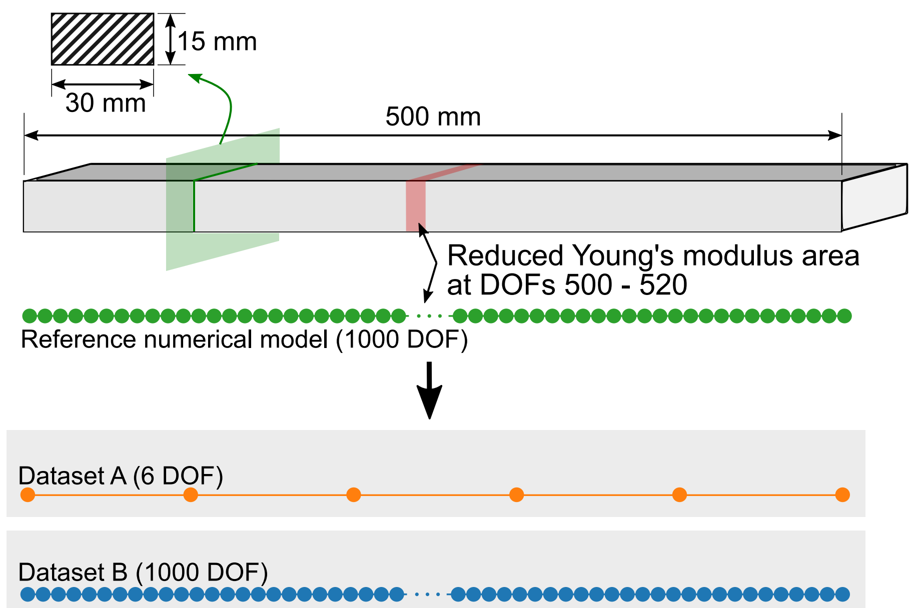

Figure 3: Beam dimensions in the reference numerical model. Translational degrees of freedom for dataset A and dataset B are presented.

From the reference numerical model, two reference datasets with the first five eigenvalues and the associated modal shapes (excluding rigid-body modes) were extracted, *i.e.*, reference datasets A and B (Fig. 3). The modal shapes in dataset A were generated in 6 translational Degrees Of Freedom

(DOFs), to simulate the spatially sparse accelerometer measurement. Modal shapes in dataset B were generated in 1000 translational DOFs, simulating the spatially dense high-speed-camera measurement. The rotational DOFs were excluded from the modal shapes. Normally distributed noise was added to the modal shapes of both datasets:

$$\hat{\boldsymbol{\phi}} = \mathbf{S} + \mathbf{N}, \tag{12}$$

where $\hat{\boldsymbol{\phi}}$ is the modal shape contaminated with noise, $\mathbf{S}$ is the modal shape without noise and $\mathbf{N}$ is the zero-mean noise signal, which was generated to obtain the desired Signal-to-Noise Ratio (SNR):

$$\mathrm{SNR}_{\mathrm{dB}} = 20\log_{10}\Big(\frac{S_{\mathrm{rms}}}{N_{\mathrm{rms}}}\Big), \tag{13}$$

where S_{rms} and N_{rms} are root mean square values of $\mathbf{S}$ and $\mathbf{N}$, respectively. Since the accelerometers have a higher dynamic range than the high-speed camera, a higher level of noise was added to the modal shapes in dataset B. The SNRs for the first five modal shapes are presented in Tab. 1 where the shapes at higher frequencies were given a lower SNR. The first four modal shapes from datasets A and B are shown in Fig. 4, where the increasing level of noise is also seen.

Table 1: Modal shape SNR [dB] for datasets A and B.

Mode nr.	A (6 DOF)	B (1000 DOF)
1	70	30
2	67	27
3	64	24
4	61	21
5	58	18

The finite-element model of the beam to be updated was the same as the reference numerical model but the reduced Young's modulus area was not simulated, making the Young's modulus uniform along the entire length of the beam.

The finite-element model was updated using the sensitivity approach, see Sec. 2.3, and the Young's moduli of all the elements were chosen as the updating parameters. In the updating procedure, the eigenvalue and modal-

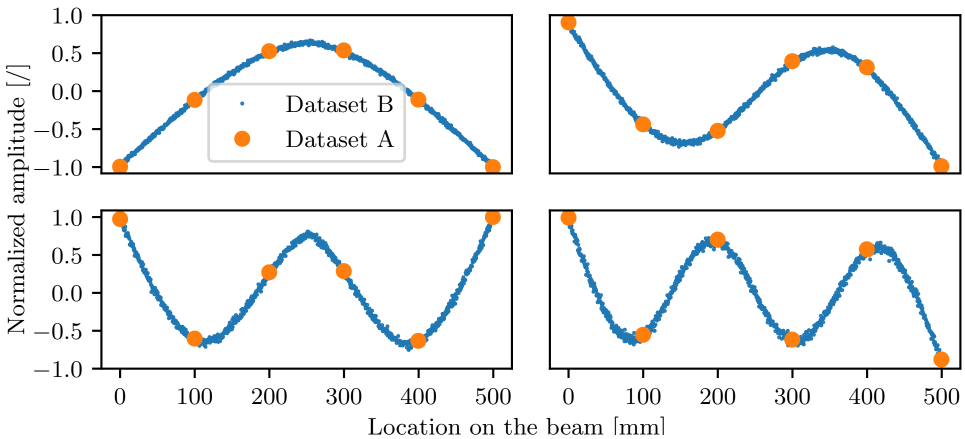

Figure 4: Modal shapes from dataset A and dataset B.

shape residuals were minimized. The eigenvalue residuals were computed as:

$$z_{\lambda,i} = \frac{\lambda_i - \hat{\lambda}_i}{\hat{\lambda}_i} \tag{14}$$

where λ_i is the i-th numerical eigenvalue and $\hat{\lambda}_i$ is the corresponding eigenvalue from the reference dataset. The difference was normalized to achieve equal weightings of all the eigenvalue residuals. The modal-shapes residuals were computed location-by-location, meaning that the amplitudes of the shape at the corresponding location were subtracted:

$$z_{\phi,i,j} = \frac{\phi_{i,j} - \hat{\phi}_{i,j}}{\sqrt{\sum_{i=1}^{n_{\mathrm{modes}}} \sum_{k=1}^{n_{\mathrm{locations}}} \hat{\phi}_{i,k}^2}}, \qquad j = 1 \ldots n_{\mathrm{locations}} \tag{15}$$

where $\phi_{i,j}$ is the i-th numerical modal shape at location j and $\hat{\phi}_{i,j}$ is the i-th modal shape from the reference dataset at the matching location. Prior to residual computation, the modal shapes were scaled using MSF, see Sec. 2.3. The first five translational eigenvalues and modal shapes were included in the updating procedure.

In the updating procedure, each mode shape ϕ_i was location weighted. Initially, the weighting was unitary:

$$w_{\varepsilon,\phi_i,j} = w, \qquad j = 1 \ldots n_{\mathrm{locations}} \tag{16}$$

where w is an arbitrary scalar weight. This unitary weighting does not take into account the large uncertainty in the DOFs close to the mode-shape nodes, where the local SNR is low, see Fig. 5. As an alternative to unitary weighting, location-specific-weighting methods were considered. The absolute and square weighting methods were studied. The absolute weighting

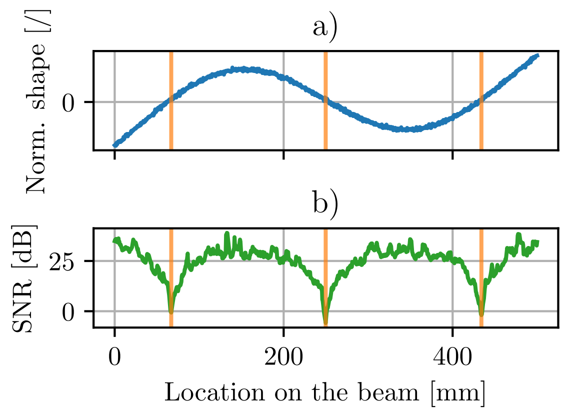

Figure 5: a) normalized modal shape from dataset B and b) local Signal-to-Noise Ratio along the beam. A moving average with a kernel size of 10 was used to compute the local SNR.

normalizes the absolute value of the shape with the Euclidean norm:

$$w_{\varepsilon,\phi_i,j} = \frac{|\phi_{i,j}|}{\sqrt{\sum_{i=1}^{n_{\text{modes}}} \sum_{k=1}^{n_{\text{locations}}} \phi_{i,k}^2}}, \qquad j = 1 \ldots n_{\text{locations}} \tag{17}$$

The square weighting normalizes the square of the shape with the Euclidean norm:

$$w_{\varepsilon,\phi_i,j} = \frac{\phi_{i,j}^2}{\sqrt{\sum_{i=1}^{n_{\text{modes}}} \sum_{k=1}^{n_{\text{locations}}} \phi_{i,k}^2}}, \qquad j = 1 \ldots n_{\text{locations}} \tag{18}$$

The weights for all the eigenvalues and modal shapes were assembled in a diagonal weighting matrix:

$$\mathbf{W}_{\varepsilon\varepsilon} = \mathrm{diag}(w_{\varepsilon,\lambda_0}, w_{\varepsilon,\lambda_1}, ..., \mathbf{w}^T_{\varepsilon,\phi_0}, \mathbf{w}^T_{\varepsilon,\phi_1}, ...) \tag{19}$$

where $w_{\varepsilon,\lambda_i}$ is the weight of eigenvalue λ_i and $\mathbf{w}_{\varepsilon,\phi_i}$ is the vector weight of modal shape $\boldsymbol{\phi}_i$, computed with Eq. (16), (17) or (18). The weight of eigenvalues $w_{\varepsilon,\lambda_i}$ were chosen as a Euclidean norm of $\boldsymbol{\phi}_i$, giving λ_i and $\boldsymbol{\phi}_i$ equal weight.

Each of the three weighting methods were used to update the finite-element model. The results in Fig. 6 show that the unitary weighting is not appropriate for the low-dynamic-range data in dataset B, since the updated Young's moduli are far from physically meaningful. For dataset A, the unitary weighting performs best; however, for dataset B, the best agreement between the updated and true values of the Young's moduli was achieved using the square weighting, see Fig. 6c.

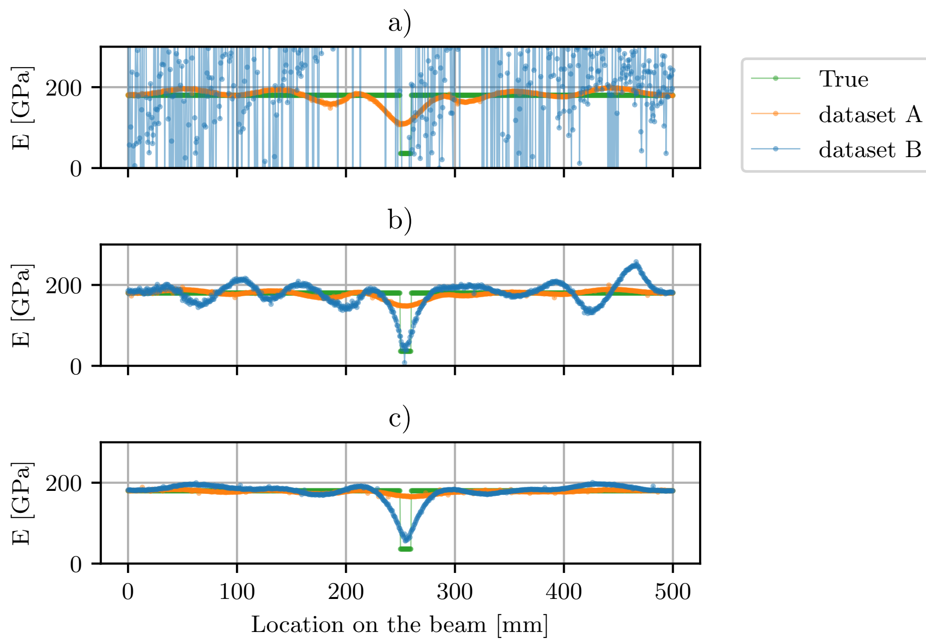

Figure 6: Young modulus along the beam as a result of different weighting methods. a) unitary, b) absolute and c) square weighting.

With dataset A, the problem of sensor location appears (due to the small number of sensors). To investigate the impact of the sensor location, the sensors in dataset A were randomly positioned along the beam. The random sensor positioning simulates the lack of knowledge regarding the optimal/best sensors positions, which is often the case for a geometrically complex structure (without preceding structural analysis). The updating results for three, random sensor positions, unitary weighting and the modal-shape noise according to Tab. 1, are shown in Fig. 7. It is clear that with the low spatial density measurement, the change in the sensor location impacts heavily on the updated parameter values. The relative uncertainty of the updated Young's moduli (Fig. 8) in the low-stiffness area of the beam (centre) is larger than 200 %, while the relative error in the same area is 55 % when dataset B was used, see Fig. 6c. Additionally, the pairing of the modal shapes from the experiment and the numerical model is subject to errors. Typically, a MAC filter is used; however, with low-spatial-density modal shapes, spatial aliasing can occur, see Sec. 2.3.

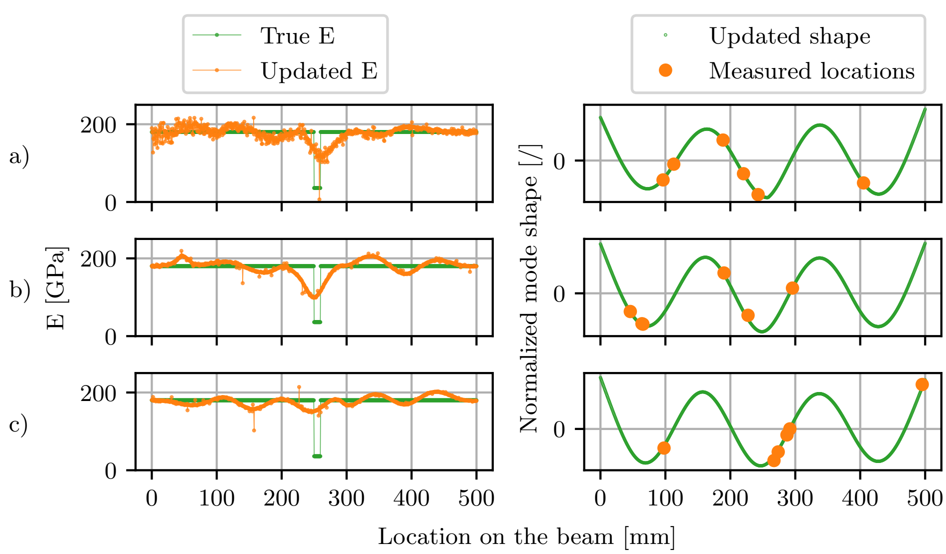

Figure 7: Dataset A - Updated Young's moduli (left) for three different (random) accelerometer positions (indicated on the right by orange dots).

With the high-spatial-density measurement (dataset B), full-field modal shapes are obtained, eliminating the sensor-location problem. Since the noise levels are usually higher in high-speed-camera measurements, the impact of the noise level was investigated. Fig. 9 shows the updated Young's moduli

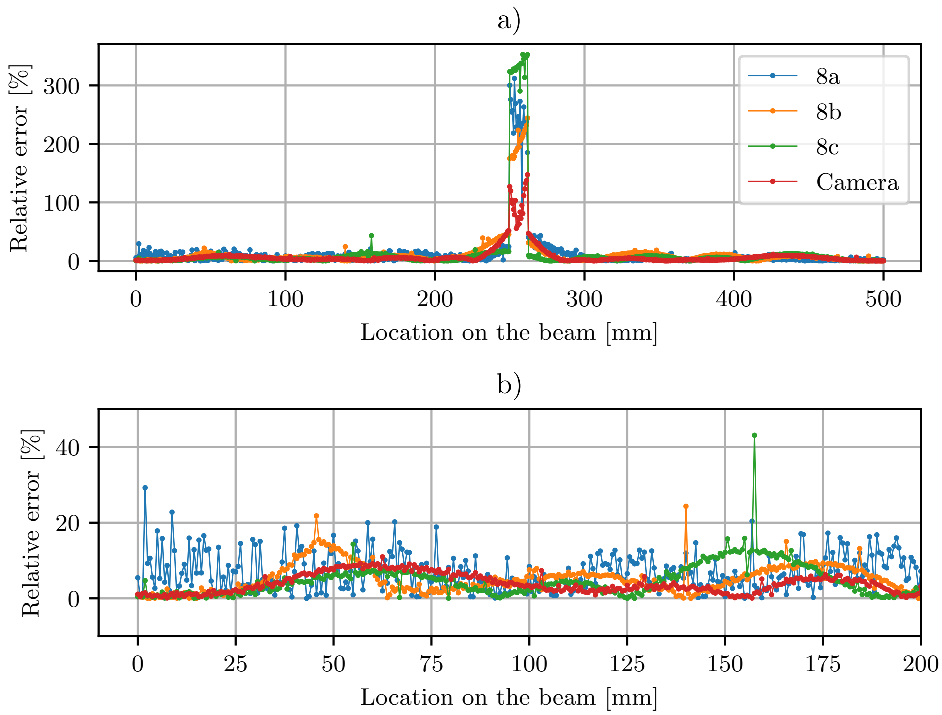

Figure 8: Relative error in updated Young's moduli along the beam for Figs. 7a, 7b, 7c and camera (Fig. 6c). a) full beam and b) zoom-in on left part of the beam.

for mode-shape SNRs of 30 dB and 20 dB (for first shape, higher shapes had lower SNRs as presented in Tab. 1), where the square weighting was used. It is clear that even with a SNR of 20 dB, the updating procedure correctly identified the low stiffness area. The parameters converged and were correctly identified over the entire length of the beam; however, some parameter deviation was introduced by the very high noise level in the 20-dB modal shape.

The updated eigenvalues, normalized to the reference values, for the best-performing weighting (dataset A with unitary weighting and dataset B with square weighting) and evenly distributed sensors in dataset A, are compared in Fig. 10. It is clear that the updated eigenvalues, along with the ones not included in the updating process, are closer to the reference values when dataset B was used.

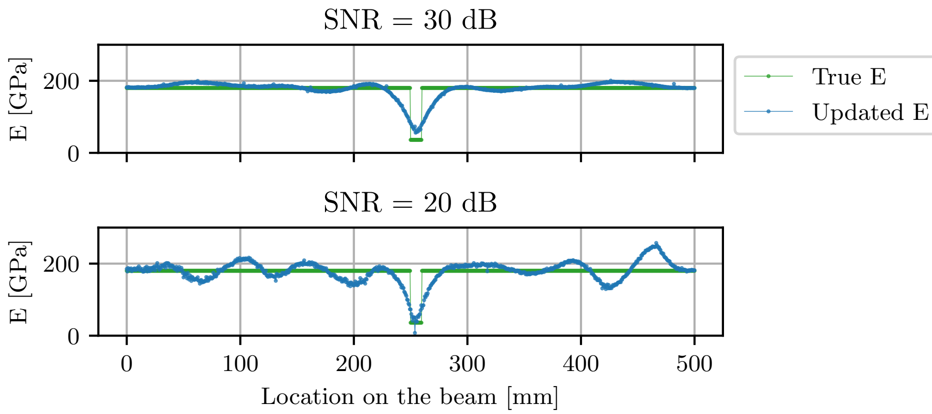

Figure 9: Dataset B - Comparison of noise effect on updated Young's moduli.

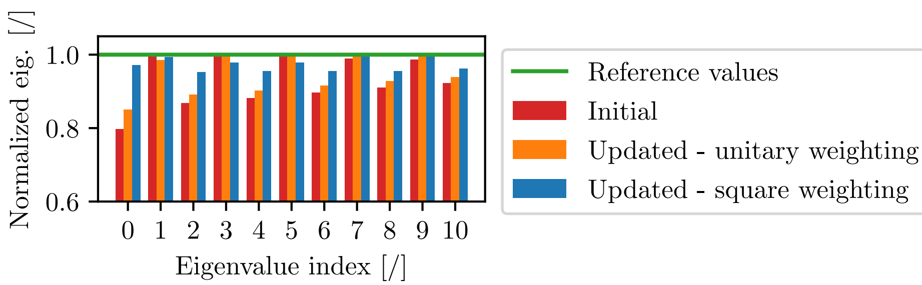

Figure 10: Comparison of normalized eigenvalues before and after updating with unitary weighting (dataset A) and square weighting (dataset B).

4. Experiment

A real experiment was carried out to obtain data for the model-updating procedure. A beam was supported by foam pads to approximate a free-free boundary condition and a notch was cut in the middle of the beam, see Fig. 11. The full experimental setup is shown in Fig. 12.

The experiment was conducted in two parts, *i.e.*, with the accelerometers and the high-speed camera. First, two accelerometers were attached to the beam (100 and 300 mm from the left edge) and a modal hammer, with a roving-hammer technique was used to excite the beam in the vertical direction at 9 locations, equally spaced at every 50 mm. The acceleration and force measurements were 1 second long and the sampling frequency was

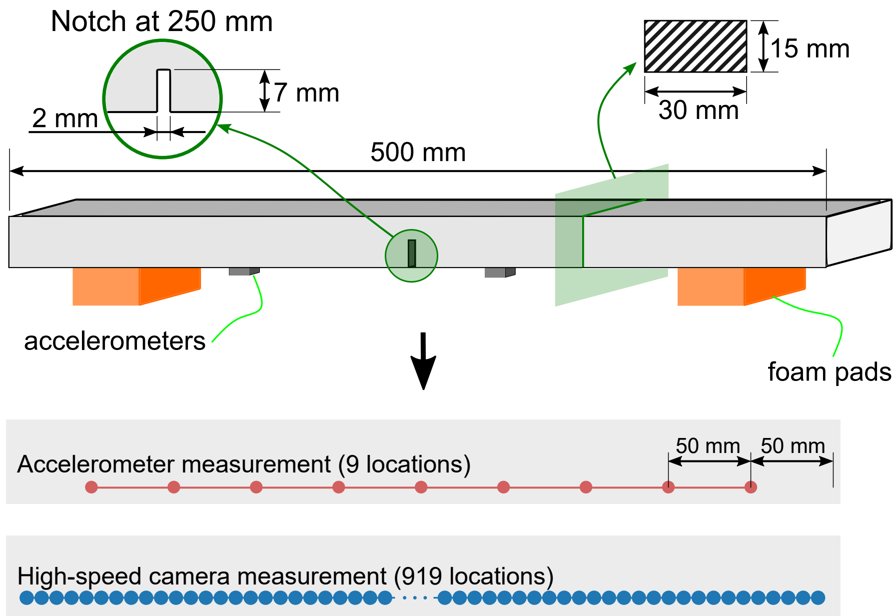

Figure 11: Experimental setup of a beam with a notch.

51 200 Hz. The FRF estimates were computed and an open-source Python package pyEMA [54] was used to obtain the modal parameters.

Second, a Photron FastCam SA-Z high-speed camera was used to measure the response of the beam. The accelerometers were kept attached and a speckle pattern was applied to the front face of the beam, see Sec. 2.1. A Sigma lens (focal length 50 mm and f2.8) was used, the field of view was 72 $\times$ 1024 px (37.113 $\times$ 527.835 mm) and the region of interest was 29 $\times$ 970 px (14.948 $\times$ 500.000 mm). The approximate distance from the camera to the beam was 115 cm and the image scale was 0.515464 mm/px. Powerful flickerless LED lights were used to illuminate the surface of the beam and a black screen was placed behind the beam to eliminate the background reflections. A modal hammer was used to excite the structure in the vertical direction, at a single location (100 mm from the left-hand edge) the responses were captured simultaneously for roughly 7000 locations on the beam, see Fig. 13. The frame rate of the camera was 100 000 frames per second and the measurement duration was 1 second. The sampling frequency of the force measurement from the modal hammer was 51 200 Hz; the measurement duration was also 1 second. The difference in the sampling frequency was resolved in the frequency domain; since sampling time was the same for both

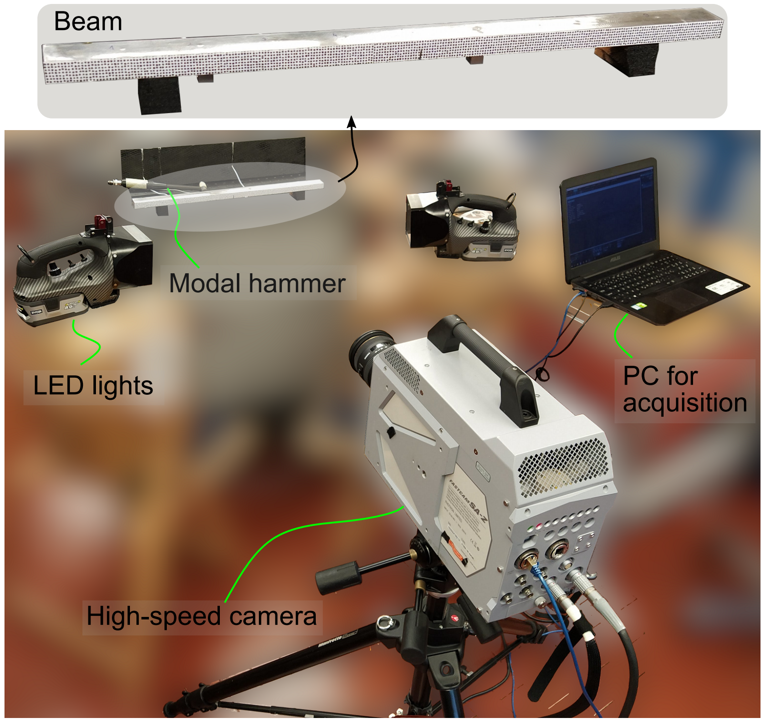

Figure 12: Experimental setup of a beam and a high-speed camera.

measurements the frequency resolution was also the same. The observed frequency range in this research was up to 2000 Hz; however, a high sampling frequency was used to capture a large number of samples in the transient response of the structure (excitation with modal hammer), improving the SNR. To identify the displacements of the beam, an open-source Python package pyIDI [64] was used, with a DIC algorithm that tracks only the rigid translations of the subsets (Sec. 2.1). The displacements were identified at 7352 locations on the beam (a regular grid of 8×919), using a subset size of 31×31 pixels. To reduce the noise, averaging of the points at the same length of the beam was used, resulting in 919 locations along the beam's length. Since the excitation was applied in the vertical direction and the horizontal displacements were deemed negligible, only vertical displacements were analysed. The modal parameters were extracted using pyEMA, where the poles from the acceleration measurement were used to reconstruct the full-field modal shapes, see the hybrid method in Sec. 2.2. The modal shapes obtained from the accelerometer and the high-speed-camera measurements are shown in Fig. 14. It is clear that the noise level was exaggerated for the modal shapes studied in the previous section, see Fig. 4, since the high-speed-camera modal shapes (Fig. 14) are less noisy.

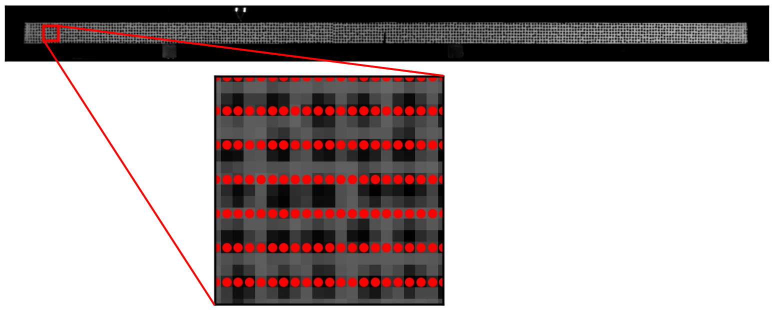

Figure 13: First frame from camera and the centres of the subsets.

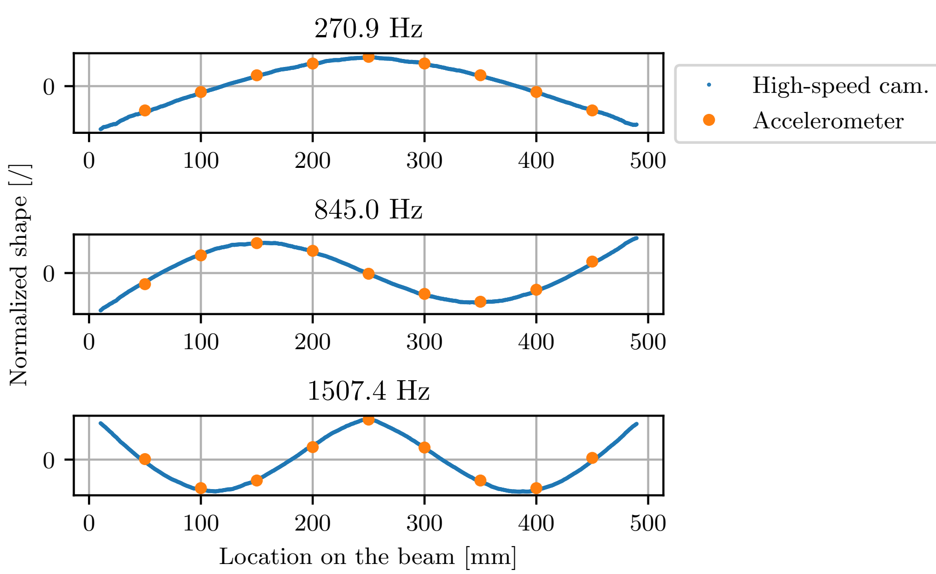

Figure 14: Measured modal shapes from accelerometers and high-speed camera.

The finite-element model to be updated was defined with 999 Timoshenko finite elements [65]. The free-free boundary condition was applied and the dimensions of the beam were assumed to be known (Fig. 11). The density of the material, ρ, was 7400 kg/m^3, the Young's modulus, E, was 180 GPa and the Poisson's ratio, ν, was 0.3. The Timoshenko shear coefficient, κ, was 5/6. The two accelerometers were modelled as point masses with a mass of 4 grams. The height of every element was updated, but no information about the location or depth of the notch was included in the initial parameter values. Additionally, a single Young's modulus (homogeneous material was assumed) was updated for all the elements. ρ, ν and κ were constant for all elements. It is worth noting that a modelling error was introduced, since the notch on the real beam was cut on one side only, while the numerical model simulated the notch on both sides.

The updating procedure was carried out as described in Sec. 3. The accelerometer mode shapes were weighted using the unitary weighting and the high-speed-camera shapes with the square weighting. Only the first three eigenvalues and modal shapes were included in the residual vector.

The results in Fig. 15a show that the updating procedure using low-spatial-density modal shapes from the accelerometers detected the approximate location of the notch, but did not successfully identify its depth. On the other hand, when using the high-spatial-density modal shapes from the high-speed camera, the location and depth of the notch were successfully identified (Fig. 15b). Furthermore, the updated height at the edges of the beam is closer to the true value when using the high-speed-camera measurement. One can notice the increased height of the beam in the area near the notch, especially in Fig. 15b, a consequence of the modelling that causes a difference in the stress field (1D Timoshenko beam elements assume symmetrical reduction in height). In the updating procedure with the accelerometer modal shapes, a lower Young's modulus (Tab. 2) compensated for the poor identification of the depth of the notch. The updating procedure with the accelerometer approach reached 90% of the final cost in 38 iterations, while with the high-speed camera approach the 90% of the final cost was reached in 47 iterations. The final number of iterations was 49 and 60 for the accelerometer and high-speed camera approach, respectively.

The eigenvalues of the updated model are compared to the initial and reference values in Fig. 16. It is clear that the high-speed camera modal shapes were better able to reproduce the reference eigenvalues than the accelerometer modal shapes. The small errors in the updated eigenvalues that were not included in the updating procedure (only the first three eigenvalues and modal shapes were included) indicates that the updated parameters are consistent with the observed structure.

Table 2: Young modulus of the beam, E [GPa].

	Initial	Updated	True
Accelerometers	180	148.392	∼190
High-speed camera	180	184.767	∼190

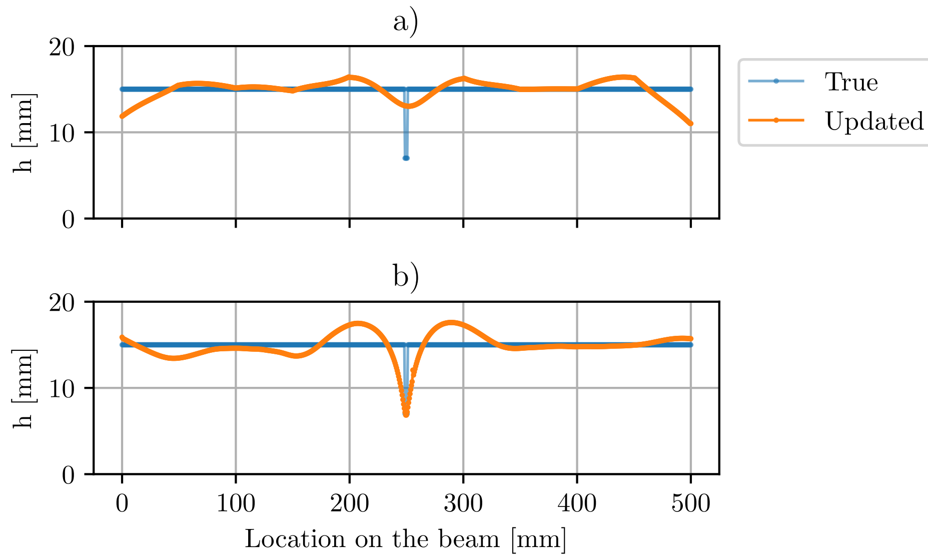

Figure 15: Initial, updated and true beam-height distribution. a) modal shapes with 9 locations from the accelerometers and b) modal shapes with 919 locations from the high-speed camera.

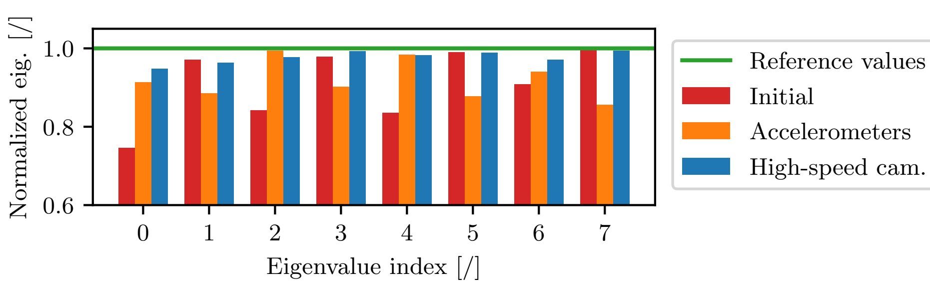

Figure 16: Comparison of the initial and updated normalized eigenvalues.

5. Conclusions

This study researches finite-element-model updating of a large number of localized parameters using full-field modal shapes.

Initially, a numerical experiment, with the simulated measurement conditions well defined and the true parameter values known was researched. It was shown that squared, location-specific weighting of the modal shapes significantly improves the identification process. Furthermore, it was shown that, due to high spatial density, the high-speed camera approach, is not exposed to the sensor location problem.

The findings from the numerical experiment were confirmed by the real experiment, where the noise levels are not predictable and the real values of the parameters are unknown. This research showed that a reduced Young's modulus area and a notch were successfully identified with no prior knowledge of the anomaly location included. The eigenvalues, reconstructed using the updated parameters with high-spatial-density modal shapes (high-speed camera) are closer to the measured eigenvalues than the eigenvalues reconstructed using the parameters from the low-spatial-density modal shapes (*e.g.* accelerometers). This is true even for the eigenvalues that were not included in the updating procedure.

Despite the lower dynamic range of the high-speed-camera measurements, compared to the accelerometer measurement, the full-field modal shapes enable the updating of a large number of localized parameters.

Acknowledgement

The authors acknowledge the partial financial support from the Slovenian Research Agency (research projects N2-0144 and J2-1730).

References

[1] Bruce D. Lucas and Takeo Kanade. An Iterative Image Registration Technique with an Application to Stereo Vision. In *Proceedings of the 7th International Joint Conference on Artificial Intelligence - Volume 2*, IJCAI'81, pages 674–679, San Francisco, CA, USA, 1981. Morgan Kaufmann Publishers Inc.

[2] W. H. Peters and W. F. Ranson. Digital Imaging Techniques In Experimental Stress Analysis. *Optical Engineering*, 21(3):213427, jun 1982.

[3] Bing Pan. Digital image correlation for surface deformation measurement: historical developments, recent advances and future goals. *Measurement Science and Technology*, 29(8):82001, 2018.

[4] Christopher Niezrecki, Peter Avitabile, Christopher Warren, Pawan Pingle, and Mark Helfrick. A review of digital image correlation applied to structural dynamics. *AIP Conference Proceedings*, 1253:219–232, 2010.

[5] Javad Baqersad, Peyman Poozesh, Christopher Niezrecki, and Peter Avitabile. Photogrammetry and optical methods in structural dynamics – A review. *Mechanical Systems and Signal Processing*, 86:17–34, 2017.

[6] Mark N. Helfrick, Christopher Niezrecki, Peter Avitabile, and Timothy Schmidt. 3D digital image correlation methods for full-field vibration measurement. *Mechanical Systems and Signal Processing*, 25(3):917–927, 2011.

[7] D. Gorjup, J. Slavič, and Miha Boltežar. Frequency domain triangulation for full-field 3D operating-deflection-shape identification. *Mechanical Systems and Signal Processing*, 133, 2019.

[8] Franck Renaud, Stefania Lo Feudo, Jean-Luc Dion, and Adrien Goeller. 3D vibrations reconstruction with only one camera. *Mechanical Systems and Signal Processing*, 162:108032, 2022.

[9] Sandro Barone, Paolo Neri, Alessandro Paoli, and Armando Viviano Razionale. Low-frame-rate single camera system for 3D full-field high-frequency vibration measurements. *Mechanical Systems and Signal Processing*, 123:143–152, 2019.

[10] Luis Felipe-Sesé, Ángel J. Molina-Viedma, Elías López-Alba, and Francisco A. Díaz. FP+DIC for low-cost 3D full-field experimental modal analysis in industrial components. *Mechanical Systems and Signal Processing*, 128:329–339, 2019.

[11] J. Javh, J. Slavič, and M. Boltežar. Experimental modal analysis on full-field dslr camera footage using spectral optical flow imaging. *Journal of Sound and Vibration*, 434:213–220, 2018.

[12] D. Gorjup, J. Slavič, A. Babnik, and M. Boltežar. Still-camera multiview Spectral Optical Flow Imaging for 3D operating-deflection-shape identification. *Mechanical Systems and Signal Processing*, 152:107456, 2021.

[13] Yen Hao Chang, Weizhuo Wang, Jen Yuan Chang, and John E. Mottershead. Compressed sensing for OMA using full-field vibration images. *Mechanical Systems and Signal Processing*, 129:394–406, 2019.

[14] Muhammad Danial Bin Abu Hasan, Zair Asrar Bin Ahmad, Mohd Salman Leong, and Lim Meng Hee. Automated harmonic signal removal technique using stochastic subspace-based image feature extraction. *Journal of Imaging*, 6(3), 2020.

[15] Roberto Del Sal, Loris Dal Bo, Emanuele Turco, Andrea Fusiello, Alessandro Zanarini, Roberto Rinaldo, and Paolo Gardonio. Structural vibration measurement with multiple synchronous cameras. *Mechanical Systems and Signal Processing*, 157:107742, 2021.

[16] Jiasheng Huang, Kuanyong Zhou, Wei Chen, and Hanwen Song. A preprocessing method for digital image correlation on rotating structures. *Mechanical Systems and Signal Processing*, 152:107494, 2021.

[17] Tino Wollmann, Edmund Koch, Julian Lich, Max Vater, Robert Kuschmierz, Christian Schnabel, Jürgen Czarske, Angelos Filippatos, and Maik Gude. Motion blur suppression by using an optical derotator for deformation measurement of rotating components. In *Nondestructive Characterization and Monitoring of Advanced Materials, Aerospace, Civil Infrastructure, and Transportation XIV*, volume 11380, page 1138016. International Society for Optics and Photonics, 2020.

[18] Ashim Khadka, Benjamin Fick, Arash Afshar, Massoud Tavakoli, and Javad Baqersad. Non-contact vibration monitoring of rotating wind turbines using a semi-autonomous UAV. *Mechanical Systems and Signal Processing*, 138:106446, 2020.

[19] Tengjiao Jiang, Gunnstein Thomas Frøseth, Anders Rønnquist, and Egil Fagerholt. A robust line-tracking photogrammetry method for uplift measurements of railway catenary systems in noisy backgrounds. *Mechanical Systems and Signal Processing*, 144:106888, 2020.

[20] Sutanu Bhowmick, Satish Nagarajaiah, and Zhilu Lai. Measurement of full-field displacement time history of a vibrating continuous edge from video. *Mechanical Systems and Signal Processing*, 144:106847, 2020.

[21] Marius Tarpø, Tobias Friis, Christos Georgakis, and Rune Brincker. Full-field strain estimation of subsystems within time-varying and nonlinear systems using modal expansion. *Mechanical Systems and Signal Processing*, 153, 2021.

[22] R. Chabrier, E. Sadoulet-Reboul, G. Chevallier, E. Foltête, and T. Jeannin. Full-field measurements with Digital Image Correlation for vibro-impact characterisation. *Mechanical Systems and Signal Processing*, 156:107658, 2021.

[23] Zhong Rong Lu, Guanfu Lin, and Li Wang. Output-only modal parameter identification of structures by vision modal analysis. *Journal of Sound and Vibration*, 497:115949, 2021.

[24] Michael Friswell and John E Mottershead. *Finite element model updating in structural dynamics*, volume 38. Springer Science & Business Media, 2013.

[25] Hongping Zhu, Jiajing Li, Wei Tian, Shun Weng, Yuancheng Peng, Zixiang Zhang, and Zhidan Chen. An enhanced substructure-based response sensitivity method for finite element model updating of large-scale structures. *Mechanical Systems and Signal Processing*, 154:107359, 2021.

[26] Mohammad Rezaiee-Pajand, Alireza Entezami, and Hassan Sarmadi. A sensitivity-based finite element model updating based on unconstrained optimization problem and regularized solution methods. *Structural Control and Health Monitoring*, 27(5):1–29, 2020.

[27] Maria Girardi, Cristina Padovani, Daniele Pellegrini, and Leonardo Robol. A finite element model updating method based on global optimization. *Mechanical Systems and Signal Processing*, 152:107372, 2021.

[28] Hua-Ping Wan and Wei-Xin Ren. Parameter Selection in Finite-Element-Model Updating by Global Sensitivity Analysis Using Gaussian Process Metamodel. *Journal of Structural Engineering*, 141(6):04014164, 2015.

[29] Roberto Rocchetta, Matteo Broggi, Quentin Huchet, and Edoardo Patelli. On-line Bayesian model updating for structural health monitoring. *Mechanical Systems and Signal Processing*, 103:174–195, mar 2018.

[30] Ayan Das and Nirmalendu Debnath. A Bayesian model updating with incomplete complex modal data. *Mechanical Systems and Signal Processing*, 136, 2020.

[31] Edoardo Patelli, Yves Govers, Matteo Broggi, Herbert Martins Gomes, Michael Link, and John E. Mottershead. Sensitivity or Bayesian model updating: a comparison of techniques using the DLR AIRMOD test data. *Archive of Applied Mechanics*, 87(5):905–925, may 2017.

[32] E.L. Zhang, Pierre Feissel, and Jérôme Antoni. A comprehensive bayesian approach for model updating and quantification of modeling errors. *Probabilistic engineering mechanics*, 26(4):550–560, 2011.

[33] K. Zhou and J. Tang. Structural model updating using adaptive multi-response Gaussian process meta-modeling. *Mechanical Systems and Signal Processing*, 147:107121, 2021.

[34] Zhiyuan Xia, Aiqun Li, Huiyuan Shi, and Jianhui Li. Model updating of a bridge structure using vibration test data based on GMPSO and BPNN: case study. *Earthquake Engineering and Engineering Vibration*, 20(1):213–221, 2021.

[35] Panagiotis Seventekidis, Dimitrios Giagopoulos, Alexandros Arailopoulos, and Olga Markogiannaki. Structural Health Monitoring using deep learning with optimal finite element model generated data. *Mechanical Systems and Signal Processing*, 145:106972, 2020.

[36] Chen Yang. An adaptive sensor placement algorithm for structural health monitoring based on multi-objective iterative optimization using weight factor updating. *Mechanical Systems and Signal Processing*, 151:107363, 2021.

[37] Weizhuo Wang, John E. Mottershead, Alexander Ihle, Thorsten Siebert, and Hans Reinhard Schubach. Finite element model updating from full-field vibration measurement using digital image correlation. *Journal of Sound and Vibration*, 330(8):1599–1620, apr 2011.

[38] Jun Wei Ngan, Colin C. Caprani, and Yu Bai. Full-field finite element model updating using Zernike moment descriptors for structures exhibiting localized mode shapes. *Mechanical Systems and Signal Processing*, 121:373–388, 2019.

[39] Alessandro Zanarini. Full field optical measurements in experimental modal analysis and model updating. *Journal of Sound and Vibration*, 442:817–842, 2019.

[40] Daniel P. Rohe. Using high-resolution measurements to update finite element substructure models. In *Rotating Machinery, Vibro-Acoustics & Laser Vibrometry, Volume 7*, pages 137–148. Springer, 2019.

[41] M. Cuadrado, J. Pernas-Sánchez, J.A. Artero-Guerrero, and D. Varas. Model updating of uncertain parameters of carbon epoxy composite plates using digital image correlation for full-field vibration measurement. *Measurement*, 159:107783, 2020.

[42] B. Pan, K. Li, and W. Tong. Fast, Robust and Accurate Digital Image Correlation Calculation Without Redundant Computations. *Experimental Mechanics*, 53(7):1277–1289, sep 2013.

[43] Elizabeth MC Jones, Mark A. Iadicola, et al. A good practices guide for digital image correlation. *International Digital Image Correlation Society*, 10, 2018.

[44] Bryan L. Witt and Daniel P. Rohe. Digital Image Correlation as an Experimental Modal Analysis Capability. *Experimental Techniques*, pages 1–14, 2021.

[45] D. Lecompte, A. Smits, Sven Bossuyt, H. Sol, J. Vantomme, D. Van Hemelrijck, and A.M. Habraken. Quality assessment of speckle patterns for digital image correlation. *Optics and Lasers in Engineering*, 44(11):1132–1145, 2006.

[46] Bing Pan, Zixing Lu, and Huimin Xie. Mean intensity gradient: An effective global parameter for quality assessment of the speckle patterns used in digital image correlation. *Optics and Lasers in Engineering*, 48(4):469–477, 2010.

[47] Y. L. Dong and B. Pan. A review of speckle pattern fabrication and assessment for digital image correlation. *Experimental Mechanics*, 57(8):1161–1181, 2017.

[48] D. Gorjup, K. Zaletelj, and J. Slavič. ladisk/speckle_pattern: v1.3.1, May 2021.

[49] P. Guillaume, L. Hermans, and H. Van der Auweraer. Maximum Likelihood Identification of Modal Parameters from Operational Data. *Proceedings of the 17th International Modal Analysis Conference (IMAC17)*, pages 1887–1893, 1999.

[50] H. Van der Auweraer, Willem Leurs, Peter Mas, and Luc Hermans. Modal parameter estimation from inconsistent data sets. In *Proceedings of SPIE-The International Society for Optical Engineering*, volume 4062, 2000.

[51] Bart Cauberghe. *Applied frequency-domain system identification in the field of experimental and operational modal analysis*. PhD thesis, Vrije Universiteit Brussel, 2004.

[52] J. Javh, J. Slavič, and M. Boltežar. High frequency modal identification on noisy high-speed camera data. *Mechanical Systems and Signal Processing*, 98:344–351, 2018.

[53] Peter Verboven, Patrick Guillaume, Bart Cauberghe, Eli Parloo, and Steve Vanlanduit. Stabilization charts and uncertainty bounds for frequency-domain linear least squares estimators. *Proceedings of the 21st IMAC, Kissimmee, FL*, 2003.

[54] K. Zaletelj, T. Bregar, D. Gorjup, and J. Slavič. ladisk/pyema: v0.24, September 2020.

[55] Donald W Marquardt. An algorithm for least-squares estimation of nonlinear parameters. *Journal of the society for Industrial and Applied Mathematics*, 11(2):431–441, 1963.

[56] R. M. Lin and D. J. Ewins. Analytical model improvement using frequency response functions. *Mechanical Systems and Signal Processing*, 8(4):437–458, 1994.

[57] R. Pascual and M. Razeto. A Robust FRF-based technique for Model Updating. *Proceedings of ISMA2002*, 3:1037–1046, 2002.

[58] R. J. Allemang. The modal assurance criterion - Twenty years of use and abuse. *Sound and Vibration*, 37(8):14–21, 2003.

[59] R. J. Allemang and D. L. Brown. A correlation coefficient for modal vector analysis. *Proceedings of the first international Modal Analysis Conference*, pages 110–116, 1982.

[60] R. M. Lin, J. E. Mottershead, and T. Y. Ng. A state-of-the-art review on theory and engineering applications of eigenvalue and eigenvector derivatives. *Mechanical Systems and Signal Processing*, 138, 2020.

[61] Andrei Nikolaevich Tikhonov. On the solution of ill-posed problems and the method of regularization. In *Doklady Akademii Nauk*, volume 151, pages 501–504. Russian Academy of Sciences, 1963.

[62] Andrew Y Ng. Feature selection, l 1 vs. l 2 regularization, and rotational invariance. In *Proceedings of the twenty-first international conference on Machine learning*, page 78, 2004.

[63] O.A. Bauchau and J.I. Craig. Euler-Bernoulli beam theory. In *Structural analysis*, pages 173–221. Springer, 2009.

[64] K. Zaletelj, D. Gorjup, and J. Slavič. ladisk/pyidi: Release of the version v0.23, September 2020.

[65] J. Thomas and B.A.H. Abbas. Finite element model for dynamic analysis of Timoshenko beam. *Journal of Sound and Vibration*, 41(3):291–299, 1975.